Available online at www.sciencedirect.com

ScienceDirect

Palaeoworld 35 (2026) 201103

Palaeoworld

www.elsevier.com/locate/palwor

Orogenesis as a pacemaker for environmental and biotic restructuring around the Ediacaran–Cambrian transition

Lei Xiang [a], Shane D. Schoepfer [b], Hua Zhang [a,*]

[a] State Key Laboratory of Palaeobiology and Stratigraphy, Nanjing Institute of Geology and Palaeontology, Chinese Academy of Sciences, 39 East Beijing Road, Nanjing 210008, China

[b] Department of Geosciences and Natural Resources, Western Carolina University, 1 University Way, Cullowhee, NC 28779, USA

Received 20 September 2025; received in revised form 12 January 2026; accepted 15 March 2026
Available online 23 March 2026

Abstract

The amalgamation of Gondwana is hypothesized to have been an important impetus for the Cambrian explosion. However, more geochemical records are required to understand the details of this linkage. Here we present a series of new high-resolution lithium and carbon isotope results from around the Ediacaran–Cambrian Transition (ECT), from a well-dated continuous section in South China. The results of lithium and carbon isotopes at the Longbizui section indicate at least two parallel large negative excursion events at the base of the Cambrian (approximately 538.8 Ma) and in the middle of Cambrian Stage 2 (approximately 524 Ma). Using coupled mass-balance box models of the lithium and carbon cycles, we infer that multiple episodes of orogenesis and enhanced physical erosion associated with the amalgamation of Gondwana lowered the fraction of carbon buried organically (f_{org}) and promoted oxidation of the large dissolved organic matter reservoir by continental sulfate runoff. The coincidence of large negative excursions in lithium and carbon isotopes with mass extinction events suggests that peaks in orogenesis can directly drive catastrophic environmental conditions for metazoans via deoxygenation. Repeated elimination of the incumbent biotas set the stage for the biological innovation around the ECT. As continental erosion rates weakened but chemical weathering enhanced after the orogenic peaks, accumulation of nutrients from continental weathering could eventually re-oxygenate the ocean. As more hospitable environments developed, they supported new rounds of biotic radiation.

Keywords: Lithium isotope; erosion; continental weathering; Gondwana'samalgamation; Cambrian explosion

1. Introduction

The Cambrian explosion was one of the most spectacular biological events in Earth's history, characterized by the rapid evolutionary radiation of nearly all extant metazoan clades, increasing body size, morphological innovations, and widespread skeletal biomineralization (Cavalier-Smith, 2017; Linnemann et al., 2019). However, the evolution of metazoans in this era was not a continuous, linear process. The Cambrian explosion, which was rooted in the Ediacaran, can be divided into at least three major phases of biodiversification, which were punctuated by at least two important mass extinction events, at the base of Cambrian and again in Cambrian Stage 2 (Shu et al., 2014; Babcock et al., 2015; Zhu et al., 2019).

A combination of environmental factors, including the availability of oxygen and nutrients, were likely crucial for the rapid evolution of metazoans and the development of modern ecosystem structure. A series of anomalous

* Corresponding author.
E-mail address: hzhang@nigpas.ac.cn (H. Zhang).

https://doi.org/10.1016/j.palwor.2026.201103

environmental events, including the highest atmospheric CO_2 levels (Hearing et al., 2021) and highest seawater $^{87}Sr/^{86}Sr$ values of the whole Phanerozoic Eon (Peters and Gaines, 2012), frequent perturbation of carbon and sulfur cycles with extremely high magnitude (Maloof et al., 2010a; Shields-Zhou and Zhu, 2013; He et al., 2019), and oscillating oceanic redox conditions (Wei et al., 2020; Pruss and Gill, 2024) were intimately coincided with the Cambrian explosion. Continental weathering is a key mechanism for consuming atmospheric CO_2, redistributing mass in the Earth's exogenic system, and determining the nutrient supply to ecosystems, which in turn can promote carbon burial and oxygenation (West et al., 2005; Frings and Buss, 2019; Hilton and West, 2020). Orogenic episodes, such as those associated with the formation of the supercontinent Gondwana, have been hypothesized as a trigger for the evolutionary innovation observed around the Ediacaran–Cambrian transition (ECT), through enhanced continental erosion and chemical weathering (Squire et al., 2006; Campbell and Allen, 2008). However, owing to the lack of key evidence to constrain the timing, tempo, driver(s), and impacts of continental erosion and chemical weathering around the ECT, the causal links among active mountain building, continental weathering, and the Cambrian explosion remain poorly understood. The lithium isotope system provides a tool to explore these connections. Lithium content in silicates is one to two orders of magnitude higher than that in carbonates (Pogge von Strandmann et al., 2020). Lithium has two stable isotopes (^6Li and ^7Li), with fractionation in the upper continental crust being sensitive to the chemical weathering intensity of silicates, but insensitive to biological effects or redox conditions (Dellinger et al., 2015).

In this study, we examined the Longbizui section of the Middle Yangtze Block, characterized by a continuous sedimentary succession spanning from the upper Ediacaran through Cambrian Series 1 (538.8–521 Ma). We collected a set of high-resolution samples ranging from the upper Liuchapo Formation to the lower Niutitang Formation, and conducted an array of geochemical measurements, including major and trace elements as well as lithium and organic carbon isotopes. We used these proxies to explore the temporal evolution of continental weathering processes, to better understand the relationship between mountain-building, chemical weathering, oceanic chemistry, and the Cambrian explosion.

2. Geological setting

The South China Craton was formed via the amalgamation of the Yangtze and Cathaysia blocks during the Sibao Orogeny, in the Neoproterozoic Era (Zhao and Cawood, 2012). While the block separated from Rodinia during the late Proterozoic, the Cathaysia Block continued to receive sediment input from the continental interior of Gondwana (Wang et al., 2021). Depositional facies on the Yangtze Block around the ECT included shallow-water platform carbonates and phosphorites, as well as deep slope and basin environments (Jiang et al., 2012; Fig. 1).

The Longbizui section is located in Guzhang county of Hunan province (109°50'32.24"E, 28°29'55.06"N; Fig. 1) and represents a basinal facies on the Middle Yangtze Block. The Ediacaran–Cambrian transitional interval of the Longbizui section includes the Liuchapo Formation and overlying Niutitang Formation (Wang et al., 2012). The Liuchapo Formation is composed of gray to black, thin- to medium-bedded cherts interbedded with shales. The Niutitang Formation is primarily composed of thinly-bedded black carbonaceous mudstones and shales, interbedded with lenticular limestones and phosphorites. No erosional unconformities are apparent between the lowermost horizons recovered from the Liuchapo Formation and the top of the Niutitang Formation, suggesting continuous deposition over the interval investigated in this study. Previous zircon dating of this section (from approximately 40 m below the lithologic contact between the Liuchapo and Niutitang formations; 545.76 ± 0.66 Ma; Fig. 2; Yang et al., 2017), and from the nearby Taoying section (basal Niutitang Formation; 522.7 ± 4.9 Ma; Wang et al., 2012) suggest that the Liuchapo Formation was deposited from the late Ediacaran through the Cambrian Terreneuvian.

In this study, we followed the chemostratigraphic and biostratigraphic correlation schemes proposed by Wang et al. (2012) and Yang et al. (2017), as shown in Fig. 2 and Fig. S1, respectively. In particular, the N2 carbon isotope excursion at the Longbizui section is correlated with the basal Cambrian negative carbon isotope excursion (BACE; Shields-Zhou and Zhu, 2013; Fig. S1) that has been observed around the world (approximately 538.8 Ma). The N4 carbon isotope excursion event at the Longbizui section corresponds temporally to the negative carbon isotope excursion in the lower part of the Shiyantou Formation (SHICE) on the South China platform (Shields-Zhou and Zhu, 2013), and to the nadir of the negative excursion between I and II in Siberia (Kouchinsky et al., 2012), which was dated to the middle of Cambrian Stage 2 (approximately 524 Ma).

3. Materials and methods

In this study, we systematically sampled the Liuchapo and Niutitang formations at the Longbizui section at an average spacing of 50 cm. In total, 82 samples were collected and broken into pieces (diameter ~2 mm) using a hammer. The pieces of the crushed samples were selected to avoid veins and cavities and pulverized using a SPEX 8515 Shatterbox with a ceramic puck.

A total of ~50 mg powder sample was soaked in 1 N $MgCl_2$ (adjusted to pH = 7.0) for 8 hours, then exposed to 1N NaOAc (adjusted to pH = 5.0 with acetic acid) for 5 hours, to remove the exchangeable lithium bound to carbonate (Tessier et al., 1979). The sample was centrifuged for 15 minutes at 4000 rpm, and the supernatant was

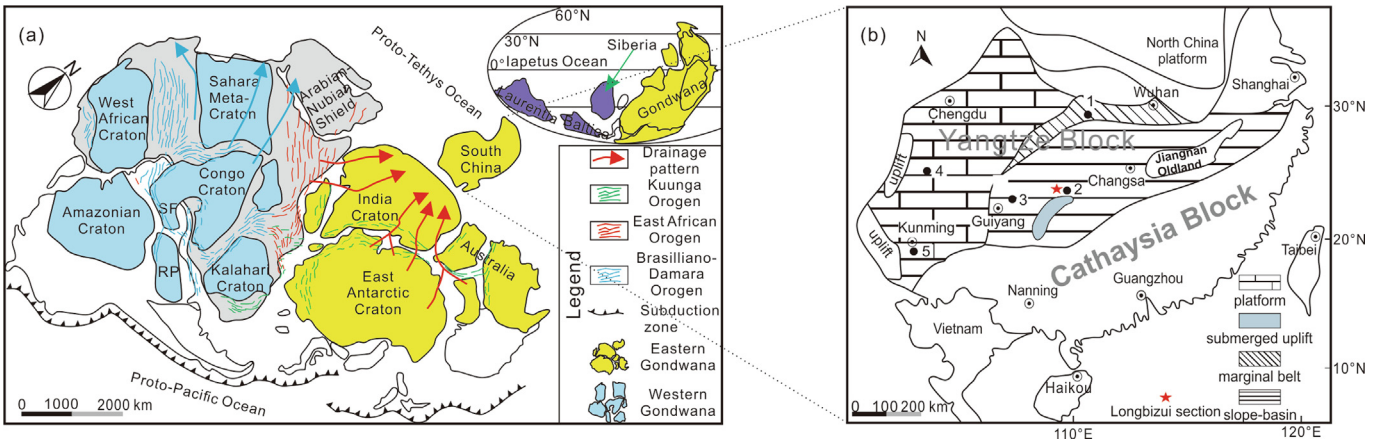

Fig. 1. Simplified paleogeography of (a) Gondwana, and (b) South China around the ECT, showing the location of Longbizui section (modified from Jiang et al., 2012; Wang et al., 2019; Liu et al., 2021). Published stratigraphic sections in (b) include: 1 – Three Gorges area, 2 – Yuanjia, 3 – Weng'an, 4 – Xiaotan, and 5 – Chengjiang.

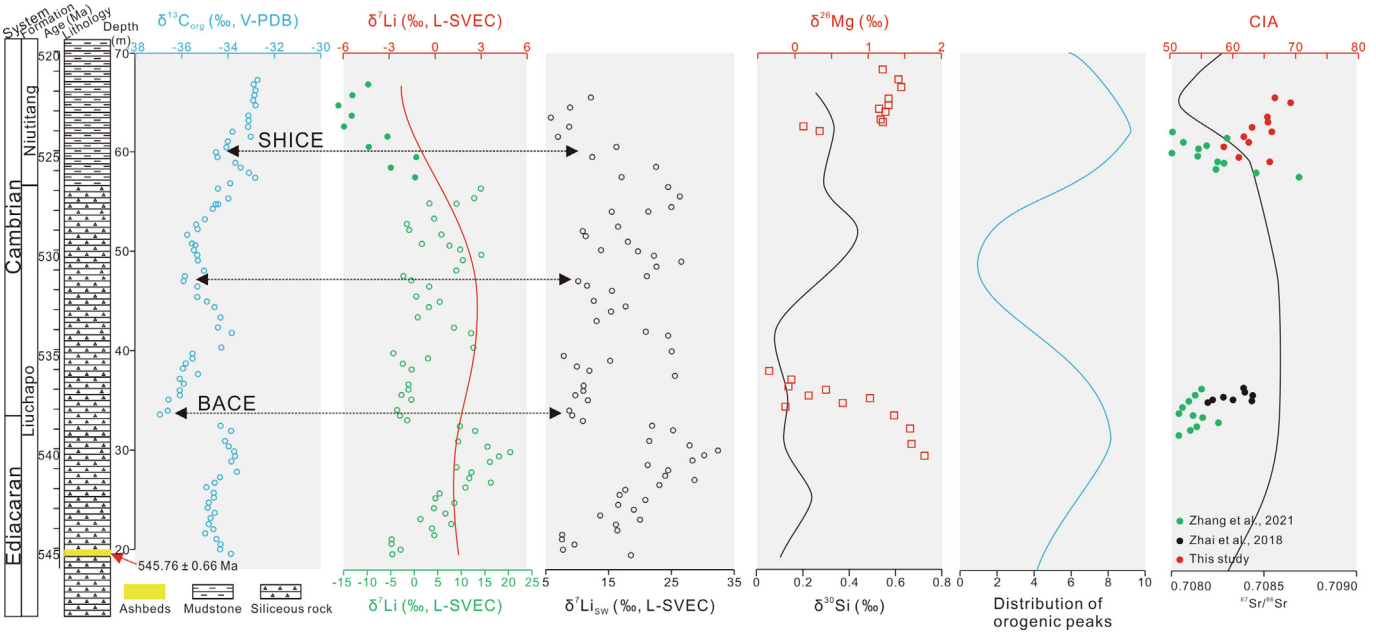

Fig. 2. Stratigraphic distribution of $\delta^{13}C_{org}$, $\delta^{7}Li$, and CIA at the Longbizui section, with a compilation of synchronous records of $\delta^{30}Si$, timing of orogenic peaks, CIA, and $^{87}Sr/^{86}Sr$. $\delta^{7}Li_{SW}$ represents the inferred seawater lithium isotope composition. References for compiled data are as follows: Red $\delta^{7}Li$ curve (Wei et al., 2024); $\delta^{30}Si$ (Ye et al., 2021); distribution of orogenic peaks (Schmitt et al., 2018); CIA (Zhai et al., 2018; Zhang et al., 2021); $^{87}Sr/^{86}Sr$ (Peters and Gaines, 2012).

discarded. The samples were subsequently washed 5 times with MQ H_2O (18.2 MΩ at 25℃). The dried residue was subsequently digested with a mixture of concentrated HF-HNO_3 using a closed vessel at a temperature of 190℃ for 72 hours. After eliminating the refractory fluorides using concentrated HNO_3 on a hot plate at 120℃, the sample was redissolved in concentrated HNO_3 for 12 hours.

A split of 50% of the clean solution was evaporated to dryness, diluted 20 times with 3% HNO_3 (v/v) and spiked with 10 ppb Re. Major and trace element concentrations (including rare earth elements) were analyzed using an Agilent 7700X quadrupole inductively-coupled plasma mass spectrometer (ICP-MS) and Agilent 710 inductively coupled plasma-optical emission spectrometer (ICP-OES) at the State Key Laboratory of Palaeobiology and Stratigraphy, Nanjing Institute of Geology and Palaeontology (NIGP), Chinese Academy of Sciences (Xiang et al., 2017).

Chemical index of alteration (CIA) is calculated using the molar proportions of each species: $CIA = (Al_2O_3)/(Al_2O_3 + CaO^* + Na_2O + K_2O) \times 100$ (Nesbitt and Young, 1982). Where CaO* represents the CaO contents in silicate fraction only and can be corrected using the following formula: $CaO^* = (CaO - P_2O_5) \times 10/3$. If the remaining value of CaO* is higher than Na_2O, the Na_2O was adopted as CaO* (McLennan et al., 1993). CIA values

at this section require a further correction for diagenetic K_2O addition, to avoid the effects of diagenetic K addition in shales (Cox et al., 1995). This amount of diagenetic K_2O addition can be estimated using the following equation from Panahi et al. (2000): $K_2O_{corr} = \text{molar}\ [m \times Al_2O_3 + -m \times (CaO^* + Na_2O)]/(1-m)$. In this equation, m is the proportion of K_2O from the parent sample and can be expressed as: $m = \text{molar}\ K_2O/(Al_2O_3 + CaO^* + Na_2O + K_2O)$.

The other 50% of the clean dissolution was used for lithium isotope analysis, following the procedures detailed by Qie et al. (2023) to separate and purify lithium and measure Li isotopes. A dual-column system, using different sizes and volumes of Bio-Rad® AG50W-X12 cation exchange resins, was used to purify lithium from the matrix. After matching the lithium concentration between samples and bracketing calibrators (L-SVEC standard, NIST SRM 8545), a standard sample bracketing method was used to correct the instrumental mass bias and blanks using the L-SVEC standard (NIST SRM 8545). Sample values were calculated based on the bracketing standard and blank values.

$$\delta^7Li = [(^7Li/^6Li)_{sample}/(^7Li/^6Li)_{L-SVEC} - 1] \times 1000\ (‰)$$

The overall reproducibility and accuracy of the lithium procedure (sample digestion, lithium separation, and isotope analysis) was checked by repeated measurements of BHVO-2 ($\delta^7Li = 4.53‰ \pm 0.37‰$, 2SD, $n = 6$), IAPSO Standard Seawater ($\delta^7Li = 31.23‰ \pm 0.40‰$, 2SD, $n = 10$), and Alfa-Lithium ($\delta^7Li = 14.39‰ \pm 0.32‰$, 2SD); the analytical results were consistent with the published values. Samples preparation, column chemistry, and lithium isotope analyses were performed at NIGP.

Analyses of carbon isotopes of organic matter were conducted following the procedure outlined in Xiang et al. (2017, 2018).

4. Models

A simple box model of the global carbon and lithium cycles was formulated to explore the mechanisms underlying the coupled lithium and carbon isotope excursions around the ECT. The model was implemented within Matlab R2020a.

The lithium mass balance models proposed by Li and West (2014) and Kalderon-Asael et al. (2021) were used as follows:

$$F_{RIV} + F_{HR} = F_{AOC} + F_{MAAC} \quad \text{(Equation 1)}$$

$$N_{SW} \times d(\delta^7Li_{SW})/dt = F_{RIV} \times (\delta^7Li_{RIV} - \delta^7Li_{SW}) + F_{HR} \times (\delta^7Li_{HR} - \delta^7Li_{SW}) + F_{AOC} \times \Delta^7Li_{AOC} + F_{MAAC} \times \Delta^7Li_{MAAC} \quad \text{(Equation 2)}$$

The sink flux of lithium from the ocean via the alteration of oceanic crust (AOC) and formation of marine authigenic aluminosilicate clays (MAAC) pathways can be calculated using the oceanic reservoir size of lithium (N_{SW}) divided by its residence time (τ_{Li}). Equation 2 can thus be rewritten as:

$$N_{SW} \times d(\delta^7Li_{SW})/dt = F_{RIV} \times (\delta^7Li_{RIV} - \delta^7Li_{SW}) + F_{HR} \times (\delta^7Li_{HR} - \delta^7Li_{SW}) + N_{SW}/\tau_{Li} \times (f_{AOC} \times \Delta^7Li_{AOC} + (1 - f_{AOC}) \times \Delta^7Li_{MAAC}) \quad \text{(Equation 3)}$$

We simplified the $f_{AOC} \times \Delta^7Li_{AOC} + (1 - f_{AOC}) \times \Delta^7Li_{MAAC}$ in Equation 3 into a single variable Δ^7Li_{sink}. Equation 3 can thus be rewritten as follows:

$$N_{SW} \times d(\delta^7Li_{SW})/dt = F_{RIV} \times (\delta^7Li_{RIV} - \delta^7Li_{SW}) + F_{HR} \times (\delta^7Li_{HR} - \delta^7Li_{SW}) + N_{SW}/\tau_{Li} \times \Delta^7Li_{sink} \quad \text{(Equation 4)}$$

We coupled this lithium isotope mass balance model with a proposed carbon isotope mass balance box model (Kump and Arthur, 1999; Li and Elderfield, 2013). In this model, the inputs of oceanic dissolved inorganic carbon were subdivided into five endmembers: oxidation of methane, oxidation of oceanic dissolved organic matter (DOM), oxidative weathering of sedimentary organic matter, tectonic outgassing of CO_2, and carbonate weathering.

$$F_{OG} + F_{CW} + F_{OW} + F_{DOM} + F_{Methane} = F_{CD} + F_{OD} \quad \text{(Equation 5)}$$

$$N_{DIC} \times d(\delta^{13}C_{DIC})/dt = F_{OG} \times (\delta^{13}C_{OG} - \delta^{13}C_{DIC}) + F_{DOM} \times (\delta^{13}C_{DOM} - \delta^{13}C_{DIC}) + F_{OW} \times (\delta^{13}C_{OW} - \delta^{13}C_{DIC}) + F_{CW} \times (\delta^{13}C_{CW} - \delta^{13}C_{DIC}) + F_{Methane} \times (\delta^{13}C_{Methane} - \delta^{13}C_{DIC}) - F_{CD} \times (\delta^{13}C_{CD} - \delta^{13}C_{DIC}) - F_{OD} \times (\delta^{13}C_{OD} - \delta^{13}C_{DIC}) \quad \text{(Equation 6)}$$

A Rayleigh distillation model between the fraction of lithium incorporated into clays and that remaining dissolved in rivers was formulated to calculate the variation in riverine lithium input flux (Rugenstein et al., 2019). Silicate weathering is the predominant mechanism responsible for the net consumption of atmospheric CO_2 (Walker et al., 1981; Kump et al., 2000). The riverine lithium input flux is assumed to be proportional to the continental silicate weathering flux (Pogge von Strandmann et al., 2017). The Rayleigh distillation function was then utilized to calculate a factor for the variation in riverine lithium input flux and to infer the silicate weathering flux and the consumption of tectonic outgassing CO_2 in the carbon isotope mass balance model.

$$\delta^7Li_{RIV} = \delta^7Li_{rock} + \Delta_{sec} \times \ln(f_{Li}) \quad \text{(Equation 7)}$$

$$F_{riv,Li} = F_{riv,Li,0} \times (F_{riv,sil}/F_{riv,sil,0}) \times [1 + (f_{Li} - f_{Li,0})] \quad \text{(Equation 8)}$$

Table 1
Definitions of the parameters used in the models.

Symbol	Description	Value	References
F_{RIV}	Lithium input flux of river	10×10^9 mol/year	Misra and Froelich, 2012
F_{HR}	Lithium input flux of hydrothermal vents	10.4×10^9 mol/year	Misra and Froelich, 2012
F_{AOC}	Lithium output flux of altered oceanic crust (AOC)		Misra and Froelich, 2012
F_{MAAC}	Lithium output flux of marine authigenic aluminosilicate clays (MAAC)		Misra and Froelich, 2012
δ^7Li_{RIV}	Lithium isotope composition of river water		
δ^7Li_{HR}	Lithium isotope composition of hydrothermal vents	8.3‰	Chan et al., 1992
Δ^7Li_{AOC}	Lithium isotope fractionation associated with uptake into AOC		
Δ^7Li_{MAAC}	Lithium isotope fractionation associated with uptake into MAAC		
N_{SW}	Inventory of seawater lithium	2.76×10^{16} mol	Li and West, 2014
τ_{Li}	Residence time of oceanic lithium	0.3×10^6 year	Misra and Froelich, 2012
δ^7Li_{SW}	Lithium isotope composition of seawater		Misra and Froelich, 2012
δ^7Li_{rock}	Lithium isotope composition of primary rock	2‰	Rugenstein et al., 2019
Δ_{sec}	Lithium isotope fractionation between riverine water and secondary lithium-containing minerals	20‰	Rugenstein et al., 2019
f_{Li}	Fraction of lithium partitioned from the bedrock into the riverine dissolved load		
$F_{riv,\ Li}$	Riverine lithium flux at the nadir of the negative lithium isotope excursion		
$F_{riv,\ Li,\ 0}$	Riverine lithium flux just prior to the negative lithium isotope excursion		
$F_{riv,\ sil}$	Riverine silicate weathering flux at the nadir of the negative lithium isotope excursion		
$F_{riv,\ sil,\ 0}$	Riverine silicate weathering flux just prior to the negative lithium isotope excursion		
F_{OG}	Flux of tectonic outgassing CO_2		
$\delta^{13}C_{OG}$	Carbon isotope composition of tectonic outgassing CO_2	-5‰	Li and Elderfield, 2013
F_{OW}	Flux of weathered organic carbon		
$\delta^{13}C_{OW}$	Carbon isotope composition of weathered organic carbon	-28.1‰	Li and Elderfield, 2013
F_{CW}	Flux of weathered carbonate		
$\delta^{13}C_{CW}$	Carbon isotope composition of weathered carbonate	1.8‰	Li and Elderfield, 2013
$F_{Methane}$	Flux of methane hydrate oxidation		
$\delta^{13}C_{Methane}$	Carbon isotope composition of methane hydrate	-60‰	Li and Elderfield, 2013
F_{DOM}	Flux of DOM oxidation		
$\delta^{13}C_{DOM}$	Carbon isotope composition of DOM	-26‰	Mackensen and Schmiedl, 2019
F_{CD}	Flux of carbonate deposition		
$\delta^{13}C_{CD}$	Carbon isotope composition of carbonate deposition		
$\Delta^{13}C_{DIC-OD}$	Carbon isotope difference between oceanic dissolved inorganic carbon and burial organic carbon	27.5‰	Kump and Arthur, 1999
F_{OD}	Flux of organic carbon deposition		
$\delta^{13}C_{OD}$	Carbon isotope composition of organic carbon deposition		Li and Elderfield, 2013
N_{DIC}	Inventory of oceanic dissolved inorganic carbon	1.52×10^{19} mol	Kump and Arthur, 1999
τ_{carbon}	Residence time of oceanic dissolved inorganic carbon	1×10^5 year	Kump and Arthur, 1999
$\delta^{13}C_{DIC}$	Carbon isotope composition of oceanic dissolved inorganic carbon		

More details about the parameters, implementation and sensitivity test of the coupled lithium-carbon models were presented in Table 1 and Supplementary data.

5. Results

Organic carbon isotope ($\delta^{13}C_{org}$) values of cherts in the Liuchapo Formation range from -37.0 to -33.6‰, with an average value of -35.1‰. However, the carbon isotope composition of organic matter in the Niutitang Formation is relatively heavier, ranging from -34.5 to -32.8‰ (average of -33.4‰; Figs. 2, 3; Table S1). The lithium isotope (δ^7Li) values of the Liuchapo Formation (average of 7.4‰, n = 62) are considerably heavier than those of the Niutitang Formation (average of -6.8‰, n = 10). Two of the negative shifts in lithium isotopes correspond to negative carbon isotope excursions associated with the BACE and SHICE events (Figs. 2, 3). The CIA values of the shales within the Niutitang Formation range from 47.4 to 69.1, with an average of 62.1 (Fig. 2; Table S1).

6. Discussion

6.1. Evolution of the seawater lithium isotopes from ca. 545 to 521 Ma

The average Li/Al ratio of the Liuchapo Formation (30.4) was higher than that of the Niutitang Formation (9.6), and both formations show higher ratios than upper continental crust (UCC; 0.82×10^{-3}; Rudnick and Gao, 2014) or typical igneous rocks (0.3×10^{-3}; Dellinger et al., 2017). Aluminum content in the Longbizui samples indicates that our dissolution procedure released all lithium contained in the bulk rock, including in siliciclastic phases, Fe-

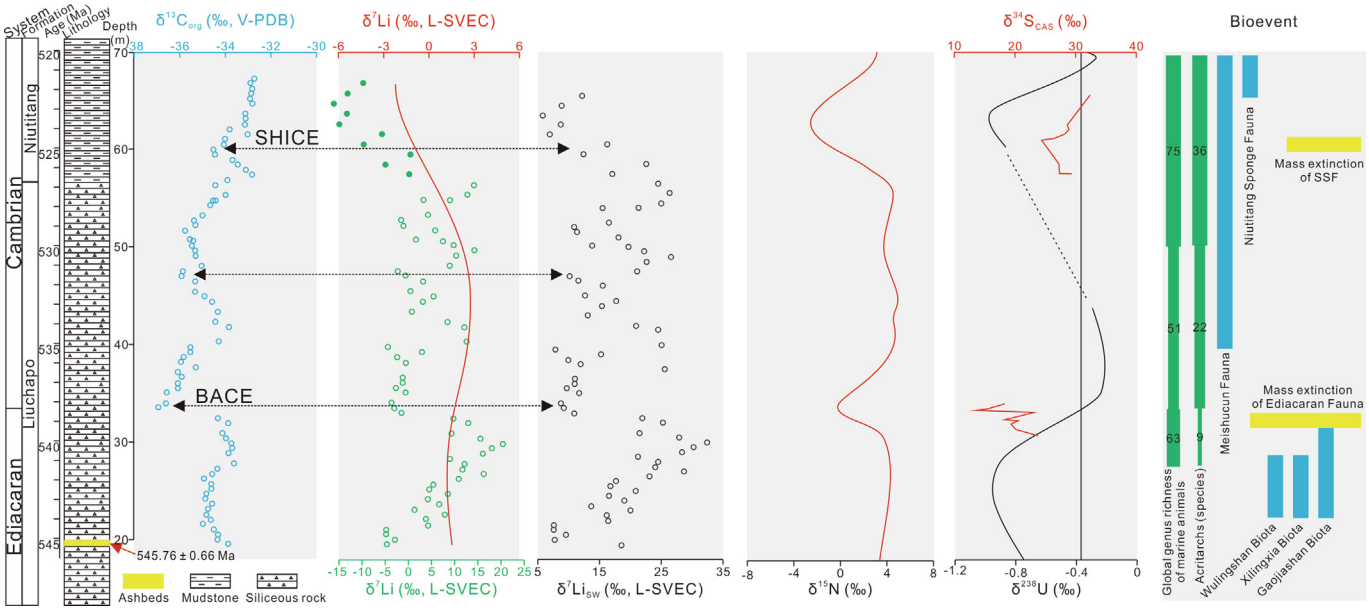

Fig. 3. Stratigraphic distribution of $\delta^{13}C_{org}$ and $\delta^{7}Li$ at the Longbizui section and a compilation of synchronous $\delta^{34}S_{CAS}$, $\delta^{238}U$, $\delta^{15}N$ results, as well as important biological events. $\delta^{7}Li_{SW}$ represents the inferred seawater lithium isotope composition. References for compiled data are as follows: Red $\delta^{7}Li$ curve (Wei et al., 2024); $\delta^{15}N$ (Wang et al., 2018); $\delta^{34}S$ of carbonate associated sulfate (CAS; Zhang et al., 2004; He et al., 2019); $\delta^{238}U$ (Zhang et al., 2018; Wei et al., 2020), and biological events (Zhu et al., 2007; Li et al., 2021).

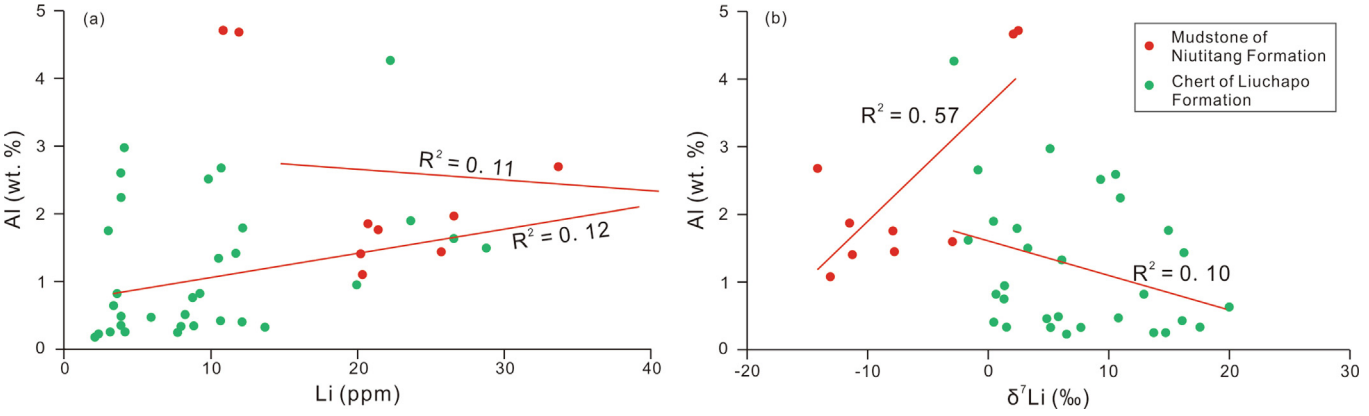

Fig. 4. Crossplots of (a) Li concentration versus Al concentration and, (b) $\delta^{7}Li$ versus Al concentration at the Longbizui section.

oxides, and chert. The weak correlation between the aluminum and lithium content and Li isotopic composition suggests that there is not a significant pool of lithium retained in the form of silicates (Fig. 4; Parnell and Armstrong, 2023), in authigenic quartz overgrowths, or as an uncharged LiOH species (Ihinger and Zink, 2000; Kolodny and Chaussidon, 2005). A previous study on the Permian-Triassic boundary indicated that the lithium isotope fractionation of chert may be similar to that of carbonate (Sun et al., 2018). The scavenging of dissolved lithium into chert in the Longbuizi depositional environment, which we hypothesize to have occurred in a relatively closed system in the opal-quartz transformation phase, may have suppressed lithium isotope fractionation (Kolodny and Chaussidon, 2005; Parnell and Armstrong, 2023).

The dominant mechanisms for lithium retention in siliciclastic rocks are either inheritance from parent rocks, or direct precipitation and crystallization associated with clay formation during continental chemical weathering and/or marine reverse weathering (Pogge von Strandmann et al., 2017; Wei et al., 2024). Various potential parent rocks in the upper continental crust, including basalts and granites, shows a limited range of variation in lithium isotopic composition, between -5 and 5‰, with an average value of 0 ± 2‰ (Sauzéat et al., 2015). The natural range of lithium isotope fractionation associated with clay formation is approximately 36‰, which is dictated by several factors, including differences in clay mineralogy, temperature, and aqueous chemistry (Hindshaw et al., 2019; Steinhoefel et al., 2021).

The striking difference in δ^7Li values between the Liuchapo and Niutitang Formations cannot be explained entirely by differences between silicate minerals in the parent rock, suggesting that the lithium isotope signal of authigenic quartz controls the variation between sections. Previous studies of lithium isotopes at marine sections show similar stratigraphic trends in δ^7Li values between marine shales and carbonates, as both lithologies accumulate lithium from the same well-mixed and uniform oceanic pool, despite different lithium isotope fractionation factors (Pogge von Strandmann et al., 2017, 2021). In this study, we interpret stratigraphic trends in δ^7Li in the chert intervals of the Liuchapo Formation to reflect coeval changes in the δ^7Li of seawater during deposition.

Following Sun et al. (2018), we assume that the lithium isotope fractionation factor between chert and seawater is similar to that between aragonite and seawater and was set to a fixed $\Delta_{\text{seawater-chert}}$ value of 9.6‰ (Pogge von Strandmann et al., 2019). Thus, the negative lithium isotope excursion corresponding to BACE represents a fluctuation from 31.9 to 6.6‰ (Figs. 2, 3). Assuming that the $\Delta_{\text{seawater-clay}}$ was 20‰ in the Niutitang Formation at the Longbizui section, we inferred that the negative lithium isotope excursion during Cambrian Stage 2 represents a fluctuation between 25.7 and 5.8‰ (Figs. 2, 3). As the tempo of excursions in lithium and carbon isotopes was approximately synchronous, the durations of the lithium isotope excursions corresponding to BACE and SHICE can be estimated as 1.33 Ma and 1.50 Ma, respectively.

6.2. *Lithium cycle perturbations driven by enhanced continental erosion*

The nadirs of all four negative excursions in reconstructed seawater lithium isotopes, including those corresponding with BACE and SHICE, were lower than 10‰. As the lithium isotope composition of the hydrothermal flux (δ^7Li_{HR}) is assumed to be constant at approximately 8.3‰ (Chan et al., 1992), a simple mass balance equation (see Supplementary data) indicates that an increase in the hydrothermal flux, even up to several orders of magnitude greater than the present value, could not reproduce the nadir of inferred seawater δ^7Li at the BACE and SHICE (Fig. 5).

The isotopic composition of seawater lithium is usually heavier than the average isotopic composition of coeval riverine lithium, owing to preferential sinks of ^{6}Li from the ocean by AOC and MAAC. Oceanic silicon concentrations, which are believed to exert a critical control on the rate of authigenic clay formation and Δ^7Li_{MAAC} values (Kalderon-Asael et al., 2021), was much higher than present levels during the terminal Ediacaran and Cambrian (Planavsky et al., 2010), as reflected by pervasive chert deposition around the ECT. Thus, the isotopic fractionations associated with lithium uptake into MAAC (Δ^7Li_{MAAC}) could not be as high as the present value (> 10‰; Misra and Froelich, 2012) during the BACE and SHICE excursions but were probably more similar to those of the Precambrian era (< 5‰, Fig. S2). Oceanic silicon concentrations declined around the ECT, corresponding to the radiation of biomineralizing organisms, including radiolarians and sponges (Conley et al., 2017). However, the trend of lithium isotopes in our study does not show any clear correlation with that of silicon isotopes (Fig. 2; Ye et al., 2021). Thus, it is unlikely that fluctuations in oceanic silicon levels around the ECT were responsible for large variations in Δ^7Li_{MAAC} and a resultant oceanic lithium isotope with a range of > 10‰.

One possible mechanism for such dramatic negative lithium isotope excursions at BACE and SHICE is a combination of extremely low riverine lithium isotope composition, and enhanced total riverine lithium input flux (see Supplementary data and Fig. 6). Modern rivers show that

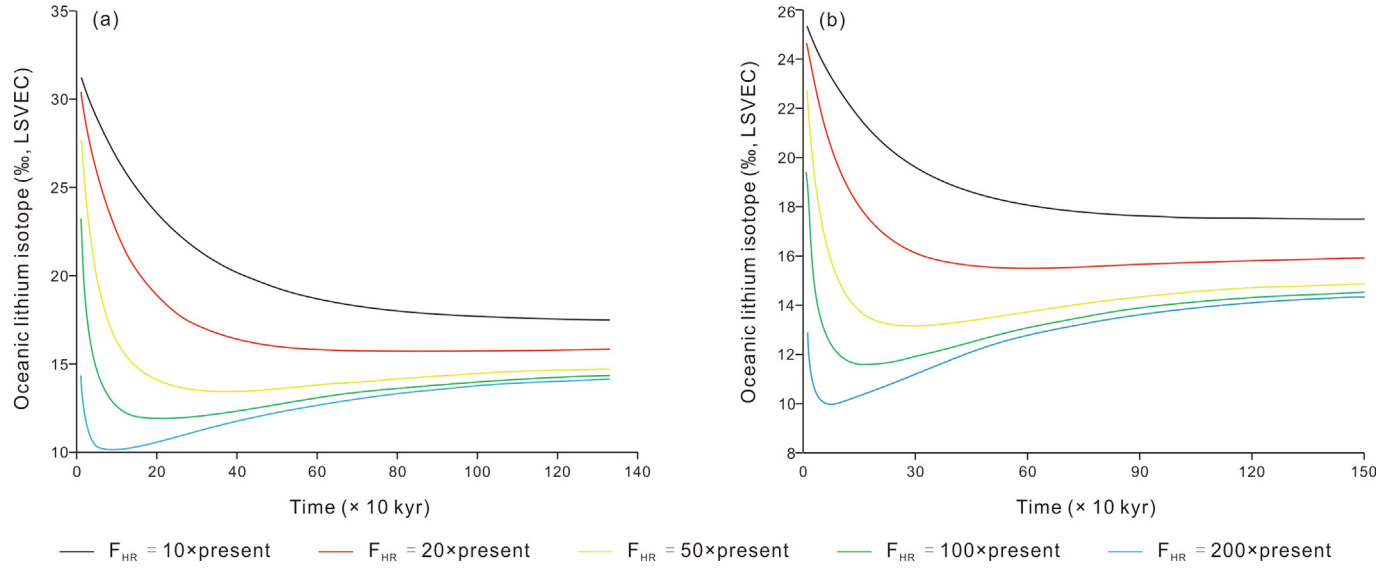

Fig. 5. Seawater δ^7Li response to increasing hydrothermal lithium flux of 10, 20, 50 and 200 times of present-day value at the (a) BACE, and (b) SHICE.

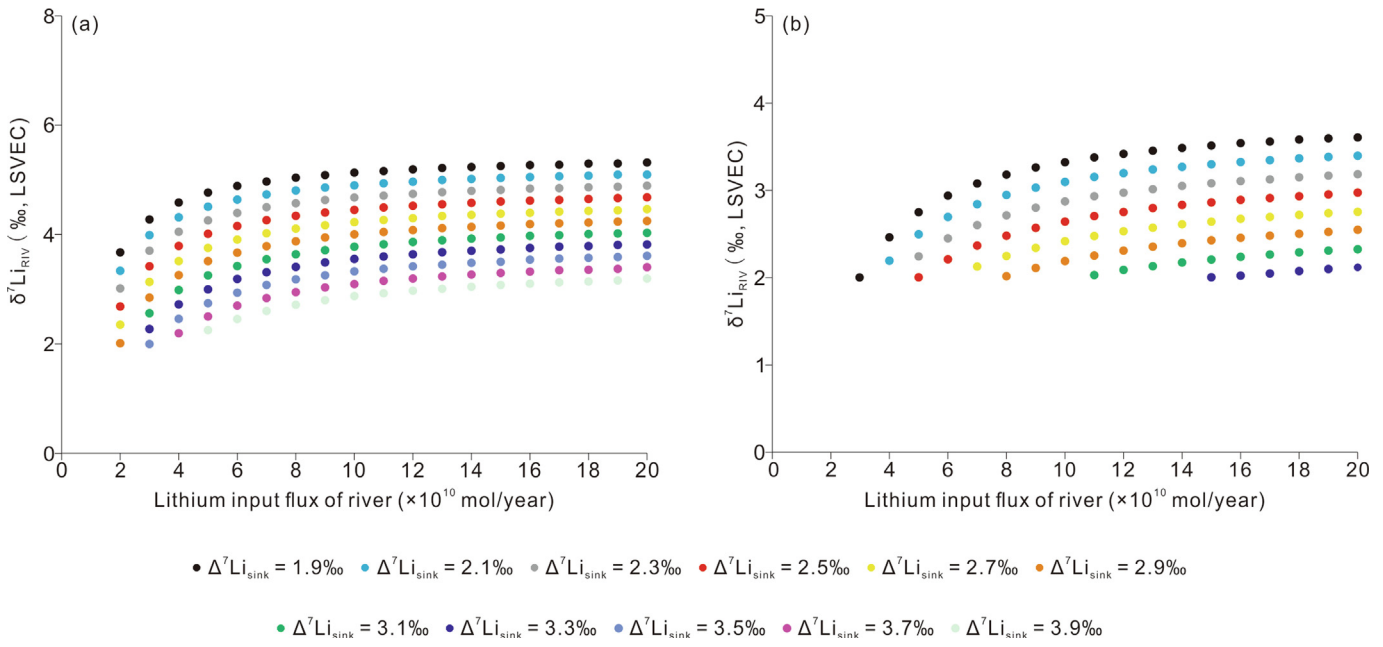

Fig. 6. Combinations of riverine δ^7Li value and corresponding riverine lithium flux to satisfy the negative δ^7Li shift at the (a) BACE, and (b) SHICE using different Δ^7Li_{sink} values ranging from 1.9‰ to 3.9‰ for (a) BACE and from 1.9 to 3.3‰ for (b) SHICE, respectively.

the weathering intensity (WI), which refers to the ratio of the weathering rate to the denudation rate, exerts a first-order influence on both the lithium flux of the riverine dissolved load and its isotopic compositions. The riverine lithium flux can increase by two to three orders of magnitude when the weathering regime changes from supply limited to kinetically limited, which implies that the WI shifts from high to low (Dixon et al., 2012; Pogge von Strandmann et al., 2021). A cross plot of riverine lithium isotopes versus WI exhibits a boomerang shape, where a positive correlation exists in the field of low to intermediate WI (< 0.05) and a negative covariation dominates in the field of intermediate to high WI (> 0.05; Dellinger et al., 2015). At the same time, the lithium isotope composition of present-day riverine waters varies from 1.3 to 43.7‰ (Huh et al., 1998). Thus, the riverine lithium content and isotopic composition can vary sufficiently to satisfy conditions for the large fluctuations around the ECT, which have characteristic time scales of < 2 Ma (Figs. 6, S1). Enhanced erosion triggered by a series of orogenic episodes associated with the assembly of Gondwana may be the most plausible explanation for the simultaneous decline of δ^7Li_{sw} and increase of riverine dissolved lithium flux at the base of the Cambrian and middle of Cambrian Stage 2 (Squire et al., 2006).

Physical erosion is accelerated by the exposure of fresh rocks on land (Molnar et al., 2007); however, the chemical weathering flux is limited by kinetic factors. Rapid erosion would also shorten the residence time of porewater fluids and reduce the amount of clay formed in these environments (Dixon et al., 2012). This in turn would decrease the amount of lithium adsorbed/incorporated in secondary clay minerals and suppress the general lithium isotope fractionation between riverine waters and parent minerals. Thus, while the WI decreases, riverine inputs of dissolved lithium to the ocean would dramatically increase as mountain building proceeds. CIA values from the shale intervals of Niutitang Formation at the Longbizui section and Bahuang section (Zhang et al., 2021), and synchronous Jiumenchong Formation at the Daotuo section (Zhai et al., 2018), show a similar vertical pattern to that of inferred seawater lithium isotope composition (Fig. 2), which corroborates our observation that nadirs in seawater lithium isotopes correspond to the lowest CIA values and weathering intensities.

The supercontinent Gondwana is believed to have developed via the suturing together of several accretionary/collisional orogenic belts, including the East African Orogen, Brasiliano-Damara Orogen, and Kuungan-Pinjarra Orogen (Zhao et al., 2018; Fig. 1a). While overall orogenesis was uninterrupted throughout the entire Ediacaran and Cambrian periods, it consisted of a series of local, episodic orogenic events on both the eastern and western margins of the incipient supercontinent, meaning the intensity of orogenic effects on geochemical cycles likely varied significantly over time.

Several discrete orogenic peaks, each with a duration of a few million years, have been recognized and arranged within a chronological sequence (Schmitt et al., 2018; Fig. 2). The distribution of these orogenic peaks around the ECT approximately tracks the distribution of excursions in our inferred seawater lithium isotope curve. The orogenic peaks between 540 Ma and 520 Ma correspond broadly to our lithium isotope excursions, and furthermore to the BACE and SHICE carbon isotope excursions. During a peak in orogenic activity, more fresh rock would be

exposed to erosion and weathering, accelerating sediment transfer from land to the ocean. This would be expressed as a massive flux of riverine lithium with low δ^7Li values, in which bedrock experienced minimal secondary fractionation of lithium owing to the relative scarcity of authigenic clay formation.

Magnesium isotopes exhibit a declining trend around the ECT, suggesting a marked attenuation in weathering intensity, which could be alternatively explained via enhanced continental erosion rather than decreased rates of chemical weathering (Zhang et al., 2021). The rapid increase in seawater $^{87}Sr/^{86}Sr$ values to their peak in the last 900 Ma also supports our interpretation that erosion, in addition to weathering, was enhanced during the Cambrian (Peters and Gaines, 2012).

6.3. Carbon cycle responses to enhanced continental erosion

A marked negative oceanic carbon isotope excursion at the base of the Cambrian (BACE) has been recorded in both organic and inorganic carbon isotopes (Maloof et al., 2010b). Through the detailed correlation of inorganic carbon isotope results from shallow-water carbonates in Mongolia, Siberia, Morocco, and South China, a rapid excursion from > 2‰ to a nadir of < -6‰ has been identified (Dahl et al., 2019). Early zircon dating from the Oman section indicated that the excursion started at 542.33 ± 0.12 Ma and peaked at 541.0 ± 0.13 Ma (Bowring et al., 2007). Thus, the duration of BACE was approximately 1.33 Ma. Similarly, a global negative carbon isotope excursion in Cambrian Stage 2 (named the negative carbon isotope shift in the Nemakit-Daldynian-Tommotian boundary section in Morocco, and SHICE in the shallow platform of South China) shifts carbonate carbon isotope values from 5‰ to -3‰ with a duration of approximately 1.5 Ma (Maloof et al., 2010a; Shields-Zhou and Zhu, 2013).

The weathering rate of carbonates is generally higher than that of silicates. As the erosion rate increases during orogenic peaks, the difference in the weathering rate between carbonate and silicate further increases (Shields and Mills, 2017). Modern regions of tectonically active mountain ranges, such as the Himalayas, show more than 75% of the total alkalinity flux derived from carbonate weathering, with the remainder derived from silicate weathering (Blum et al., 1998). At the same time, carbonate minerals typically weather congruently, with both calcium cations and carbonate anions dissolving into water (Frings and Buss, 2019). However, phosphorus-containing silicate minerals (such as apatite) in the continental crust only partially decompose as weathering proceeds. A lower WI during the orogenic peaks could result in a higher proportion of detrital phosphorus relative to dissolved (and thus potentially adsorbed) phosphorus. Many detrital phosphorus-containing minerals can be retained in floodplains and continental shelves, especially given the long distances travelled by river-transported erosion products around the ECT (Myrow et al., 2010). Therefore, detrital phosphorus cannot be effectively utilized by oceanic primary producers and contributes little to the burial flux of organic matter (Paytan and McLaughlin, 2007).

Moreover, while elevated erosion rates during orogenic peaks promote chemical weathering and increase the absolute riverine dissolved phosphorus flux (though lowering the WI), the difference in stability between carbonate and phosphorus-containing silicates could significantly lower the ratio of PO_4^{3-}/HCO_3^- in river water that reaches the ocean, causing the burial fluxes of carbonate and sedimentary organic carbon to vary disproportionately. Thus, orogenic peaks could have lowered the fraction of carbon buried as organic matter (f_{org}) and caused a negative shift in oceanic δ^{13}C values around the ECT (Maloof et al., 2010a). Conversely, owing to the different rates of weathering between carbonates and silicates, enhanced erosion during orogenic peaks would tend to increase rather than decrease the total δ^{13}C value of riverine HCO_3^- input. The increased adsorption of organic matter onto mineral surfaces (especially clays) results in a marked difference in organic carbon content between silicates and carbonate, making it impossible for accelerated oxidative weathering of organic carbon in rocks to explain the magnitude in the BACE and SHICE excursions (Zhao et al., 2023).

As the nadir of BACE is < -6‰, lower than the canonical carbon isotope composition of tectonic outgassing CO_2 (-5‰; Mason et al., 2017), such low seawater δ^{13}C values cannot be achieved by an extremely low f_{org} value (even of approximately 0). Oxidation of an organic carbon pool, either of methane hydrates or DOM, must have been involved in BACE and SHICE. The feasibility of methane oxidation for explaining the BACE and SHICE excursions is currently hindered by a dearth of reliable geological evidence, such as molar tooth structures (Shen et al., 2016), or primary carbonates with extremely negative δ^{13}C values of (< -40‰; Wang et al., 2008). Alternatively, the hypothesized existence and oxidation of a large oceanic DOM reservoir around the ECT is supported by both geological evidence and quantitative modelling (Rothman et al., 2003; Dodd et al., 2023).

Since there is a clear positive correlation between continental sulfide oxidation rate and physical erosion rate (Calmels, et al., 2007), global sulfate flux to the ocean during orogenic peaks is expected to have greatly exceeded the background level. The bottom waters of the deep ocean around the ECT were dominated by ferruginous conditions (Li et al., 2020), and the increased input of sulfate oxidant may have driven enhanced DOM oxidation via microbial sulfate reduction (MSR), leading to expansion of anoxic bottom water-masses into the photic zone at the BACE and SHICE excursions, which is supported by negative excursions in nitrogen isotopes around the world (Wang et al., 2018; Fig. 3).

As the intensity of orogenesis decreased, the overall global erosion rate would have declined relative to the rate of chemical weathering, with major implications for the phos-

phorus cycle. On a global scale, < 10% of total bioavailable phosphorus is transferred from land to the oceans as dissolved phases, with most phosphorus delivered to the ocean via clay and metal oxide particles (Froelich, 1988; Hao et al., 2021; Fru et al., 2023). When erosion rates were elevated during orogenic peaks, the formation of clays with adsorbed bioavailable P was inhibited by the decreased residence time of silicate mineral particles. In contrast, as the weathering intensity increased following orogenic peaks, more clay minerals would have been generated, and more clay-adsorbed phosphate would have been delivered into the ocean. The massive input of riverine phosphorus would promote both primary productivity and the burial of organic carbon and pyrite, driving the positive shifts in both carbon and sulfur isotopes and promoting the oxygenation of the photic zone. Studies on reactive phosphorus and micro-nutrients validate the close connection between P flux, primary productivity and carbon isotope shifts around the ECT (Cheng et al., 2020; Wei et al., in press).

Our model simulation demonstrates that, as continental weathering input increases, the amount of DOM oxidation required to achieve carbon isotope excursions of approximately -8‰ also increases (see Supplementary data and Fig. 7). As the f_{org} value decreases toward a minimum of 0.01, the amount of DOM oxidation required to explain carbon isotope excursions of -8‰ correspondingly decreases (Fig. 7). Overall, using the coupled lithium and carbon cycle model around the ECT, we conclude that the most reliable solution for the carbon-lithium isotope covariation at BACE and SHICE is a moderate increase of riverine lithium input flux (< 20× of the PAL) in combination with low δ^7Li_{riv} values (< 6‰; Figs. 6, 7, S5, S6).

6.4. Implications for the Cambrian explosion

Precipitation and temperature are two important factors affecting the continental weathering rate (West et al., 2005). Paleogeographic reconstruction shows that the major orogenic belts involved in the assembly of Gondwana were located within the low-to-mid latitude monsoon zone (Fig. 1a; Yao et al., 2021). The combination of favorable climate and widespread exposure of fresh rock could promote a rapid response between orogenesis, nutrient delivery, and biotic evolution.

The nadirs in oceanic lithium and organic carbon isotopes at the base of the Cambrian, and again at ~524 Ma, coincide with the mass extinctions of the Ediacaran fauna and small shelly fauna respectively (Babcock et al., 2015). A combination of less efficient organic matter burial, and increased oxygen consumption by DOM oxidation, would together drive deoxygenation of the Earth's surface system (Fig. 8). Uranium isotopes support oceanic anoxia during the extinction of Ediacaran metazoans and small shelly fossils (Zhang et al., 2018; Wei et al., 2020; Fig. 3). Orogenic peaks during the amalgamation of Gondwanan initially acted as a driver of mass extinctions around the ECT, through the familiar kill mechanisms of anoxia hypothesized for several of the "Big Five" mass extinctions of the Phanerozoic (Fan et al., 2020). Mass extinctions may create favorable conditions for fundamental reorganizations of the global biota, both taxonomically and ecologically (Alroy, 2008). Meanwhile, the harsh environment may stimulate the generation of morphological novelties, which in turn promote evolutionary innovation and taxonomic diversification when environmental stresses are removed (Wood and Erwin, 2018).

Carbon and lithium isotopes all show cyclical variation. The rising limb in δ^7Li and $\delta^{13}C$ at the Longbizui section reflects a rapid recovery of these elemental cycles from the effects of rapid physical erosion after the peaks in orogenesis. In the aftermath of the orogenesis peaks, the weathering regime transferred from kinetic limitation back to supply limitation (Dixon et al., 2012), with an elevated rate of chemical weathering relative to physical erosion. More clay minerals formed on the continent via chemical weathering, and more nutrients were delivered into the ocean. As organic carbon burial increased, more free oxygen accumulated in ocean-atmosphere. As metazoans need oxygen and food sources to sustain aerobic metabolism, the availability of oxygen and nutrients may have been critical determinants of early animal radiation.

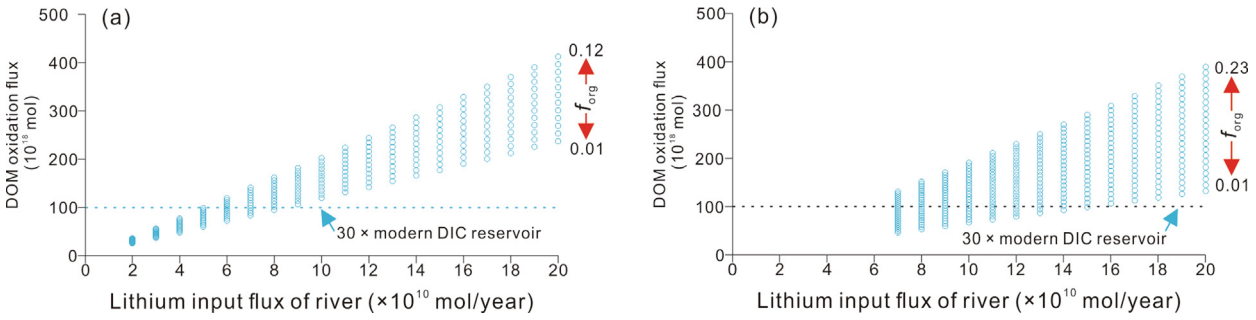

Fig. 7. Solutions for lithium-carbon covariation during the BACE and SHICE excursions across a range of riverine lithium input flux scenarios and f_{org} values. All scenarios use a typical Δ^7Li_{sink} value (2.5‰). (a) Oxidation flux of oceanic DOM required to explain the magnitude of the BACE excursion; (b) Oxidation flux of oceanic DOM required to explain the magnitude of the SHICE excursion.

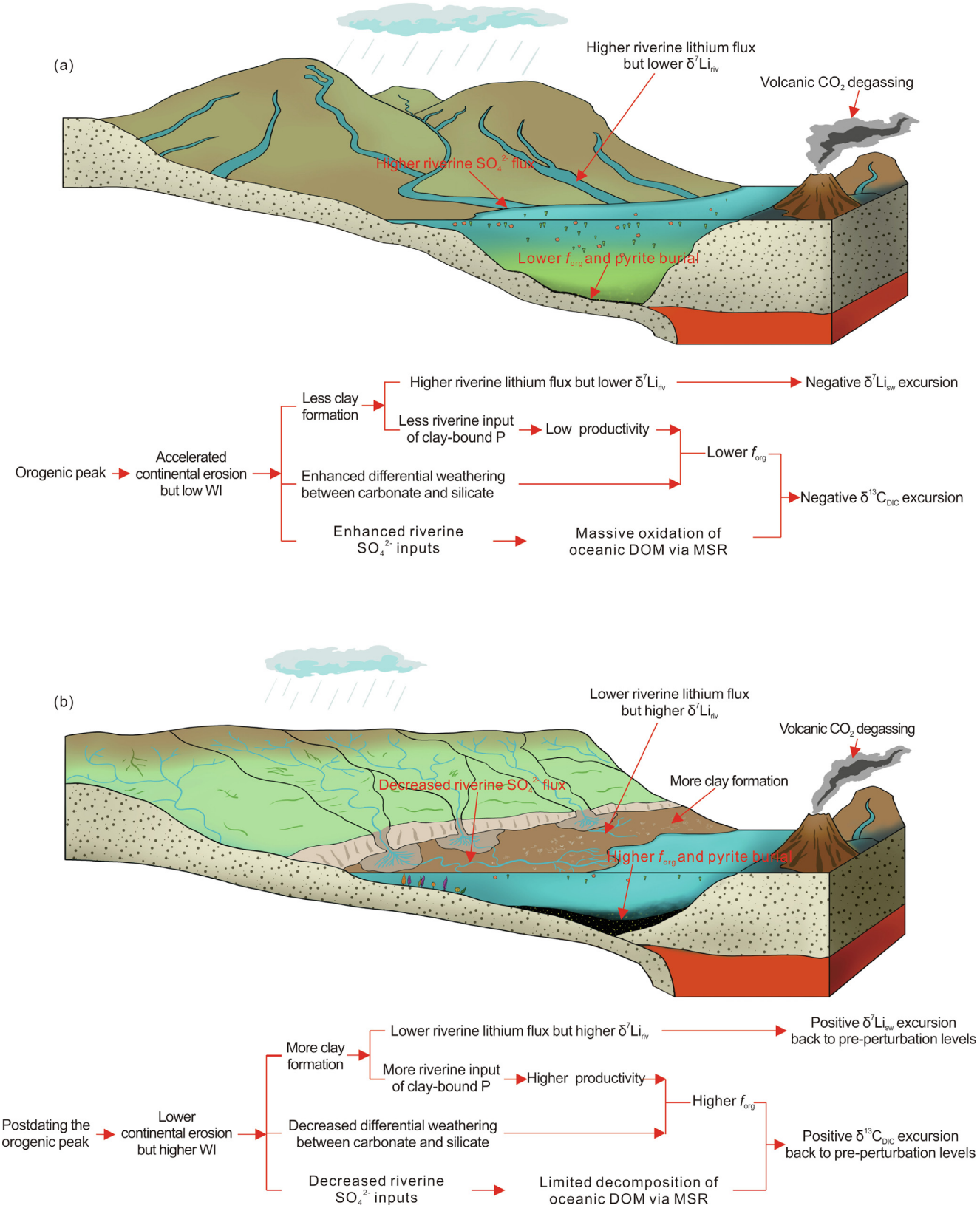

Fig. 8. Schematic model of the carbon, macronutrient, and lithium cycles during the periods of (a) orogenic peaks, and (b) postdating the orogenic peaks around the ECT.

The coincidence between a series of coupled positive excursion in seawater sulfate $\delta^{34}S$ and $\delta^{13}C_{DIC}$ and maxima in biodiversity (and habitat expansion of endemic species) around the ECT demonstrates that pulses of oxygenation may have been important time windows for the spectacular diversification of metazoans during the Ediacaran–Cambrian transition (Zhang et al., 2004; He et al., 2019; Alexander et al., 2025; Fig. 3). Collectively, mountain-building associated with the assembly of Gondwana exerted a dual impact on evolution around the ECT, with a marked time lag between the orogenic peaks and periods of biotic radiation.

7. Conclusions

We systematically sampled and analyzed carbon and lithium isotopes from the Longbizui section, South China. Our results show that extremely rapid exhumation during orogenic peaks inhibited proportional weathering and increased the rate of physical erosion relative to chemical weathering. The declining intensity of weathering during orogenic peaks lowered both the seawater lithium isotope composition and the bioavailability of phosphorus in the ocean. Increased differences in weathering congruency between carbonate and silicate minerals during the orogenic peaks, and limitation of oceanic nutrient availability, suppressed oxygenic photosynthesis and organic matter burial.

At the same time, rapid exhumation accelerated riverine sulfate flux. The combined effects of lower oxygenic photosynthesis and higher oxygen consumption led to extinctions among the incumbent biotas. As orogenesis slowed, some of these environmental stresses were alleviated, and a new episode of biotic diversification occurred. Repeated changes in environment conditions, which were in turn controlled by orogenic events on the eastern and western margins of Gondwana, may have acted as one of the key drivers for the multiple rounds of alternating extinction and origination around the ECT.

Data availability statement

Table S1 in Supplementary data contains all data used to generate plots. All data are also stored in the Science Data Bank. All samples collected as a part of this study are deposited at NIGP and can be checked.

Declaration of competing interest

The authors declare no conflict of interest relevant to this study.

Acknowledgments

This work was supported by the Strategic Priority Research Programs of the Chinese Academy of Sciences (XDB0850300). We appreciate the constructive comments from the journal editor (Prof. Zhi-Fei Zhang) and two reviewers (Prof. Jin-Long Yao and an anonymous reviewer) that helped improve the paper.

Supplementary data

Supplementary data to this article can be found online at https://doi.org/10.1016/j.palwor.2026.201103.

References

Alexander, R.D., Zhuravlev, A.Y., Bowyer, F.T., Pichevin, L., Poulton, S. W., Kouchinsky, A., Wood, R., 2025. Low oxygen but dynamic marine redox conditions permitted the Cambrian Radiation. Science Advances 11, eads2846.

Alroy, J., 2008. Dynamics of origination and extinction in the marine fossil record. Proceedings of the National Academy of Sciences of the United States of America 105, 11536–11542.

Babcock, L.E., Peng, S.C., Brett, C.E., Zhu, M.Y., Ahlberg, P., Bevis, M., Robison, R.A., 2015. Global climate, sea level cycles, and biotic events in the Cambrian Period. Palaeoworld 24, 5–15.

Blum, J.D., Gazis, C.A., Jacobson, A.D., Chamberlain, C.P., 1998. Carbonate versus silicate weathering in the Raikhot watershed within the high Himalayan crystalline series. Geology 26, 411–414.

Bowring, S.A., Grotzinger, J.P., Condon, D.J., Ramezani, J., Newall, M. J., Allen, P.A., 2007. Geochronologic constraints on the chronostratigraphic framework of the Neoproterozoic Huqf Supergroup, Sultanate of Oman. American Journal of Science 307, 1097–1145.

Calmels, D., Gaillardet, J., Brenot, A., France-Lanord, C., 2007. Sustained sulfide oxidation by physical erosion processes in the Mackenzie River basin: Climatic perspectives. Geology 35, 1003–1006.

Campbell, I.H., Allen, C.M., 2008. Formation of supercontinents linked to increases in atmospheric oxygen. Nature Geoscience 1, 554–558.

Cavalier-Smith, T., 2017. Origin of animal multicellularity: precursors, causes, consequences — the choanoflagellate/sponge transition, neurogenesis and the Cambrian explosion. Philosophical Transactions of the Royal Society B: Biological Sciences 372, 20170001.

Chan, L.H., Edmond, J.M., Thompson, G., Gillis, K., 1992. Lithium isotopic composition of submarine basalts: implications for the lithium cycle in the oceans. Earth and Planetary Science Letters 108, 151–160.

Cheng, M., Li, C., Jin, C.S., Wang, H.Y., Algeo, T.J., Lyons, T.W., Zhang, F.F., Anbar, A., 2020. Evidence for high organic carbon export to the early Cambrian seafloor. Geochimica et Cosmochimica Acta 287, 125–140.

Conley, D.J., Frings, P.J., Fontorbe, G., Clymans, W., Stadmark, J., Hendry, K.R., Marron, A.O., De La Rocha, C.L., 2017. Biosilicification drives a decline of dissolved Si in the oceans through geologic time. Frontiers in Marine Science 4, 397.

Cox, R., Lowe, D.R., Cullers, R.L., 1995. The influence of sediment recycling and basement composition on evolution of mudrock chemistry in the southwestern United States. Geochimica et Cosmochimica Acta 59, 2919–2940.

Dahl, T.W., Connelly, J.N., Li, D., Kouchinsky, A., Gill, B.C., Porter, S., Maloof, A.C., Bizzarro, M., 2019. Atmosphere-ocean oxygen and productivity dynamics during early animal radiations. Proceedings of the National Academy of Sciences of the United States of America 116, 19352–19361.

Dellinger, M., Gaillardet, J., Bouchez, J., Calmels, D., Louvat, P., Dosseto, A., Gorge, C., Alanoca, L., Maurice, L., 2015. Riverine Li isotope fractionation in the Amazon River basin controlled by the weathering regimes. Geochimica et Cosmochimica Acta 164, 71–93.

Dellinger, M., Bouchez, J., Gaillardet, J., Faure, L., Moureau, J., 2017. Tracing weathering regimes using the lithium isotope composition of detrital sediments. Geology 45, 411–414.

Dixon, J.L., Hartshorn, A.S., Heimsath, A.M., DiBiase, R.A., Whipple, K.X., 2012. Chemical weathering response to tectonic forcing: A soils perspective from the San Gabriel Mountains, California. Earth and Planetary Science Letters 323, 40–49.

Dodd, M.S., Shi, W., Li, C., Zhang, Z.H., Cheng, M., Gu, H.D., Hardisty, D.S., Loyd, S.J., Wallace, M.W., Hood, A.V., Lamothe, K., Mills, B.J.W., Poulton, S.W., Lyons, T.W., 2023. Uncovering the Ediacaran phosphorus cycle. Nature 618, 974–980.

Fan, J.X., Shen, S.Z., Erwin, D.H., Sadler, P.M., MacLeod, N., Cheng, Q. M., Hou, X.D., Yang, J., Wang, X.D., Wang, Y., Zhang, H., Chen, X., Li, G.X., Zhang, Y.C., Shi, Y.K., Yuan, D.X., Chen, Q., Zhang, L. N., Li, C., Zhao, Y.Y., 2020. A high-resolution summary of Cambrian to Early Triassic marine invertebrate biodiversity. Science 367, 272–277.

Frings, P.J., Buss, H.L., 2019. The central role of weathering in the geosciences. Elements 15, 229–234.

Froelich, P.N., 1988. Kinetic control of dissolved phosphate in natural rivers and estuaries: A primer on the phosphate buffer mechanism. Limnology and Oceanography 33, 649–668.

Fru, E.C., Al Bahri, J., Brosson, C., Bankole, O., Aubineau, J., El Albani, A., Nederbragt, A., Oldroyd, A., Skelton, A., Lowhagen, L., Webster, D., Fantong, W.Y., Mills, B.J.W., Alcott, L.J., Konhauser, K.O., Lyons, T.W., 2023. Transient fertilization of a post-Sturtian Snowball ocean margin with dissolved phosphate by clay minerals. Nature Communications 14, 8418.

Hao, W.D., Mänd, K., Li, Y.H., Alessi, D.S., Somelar, P., Moussavou, M., Romashkin, A.E., Lepland, A., Kirsimäe, K., Planavsky, N.J., Konhauser, K.O., 2021. The kaolinite shuttle links the Great Oxidation and Lomagundi events. Nature Communications 12, 2944.

He, T.C., Zhu, M.Y., Mills, B.J.W., Wynn, P.M., Zhuravlev, A.Y., Tostevin, R., Pogge von Strandmann, P.A., Yang, A.H., Poulton, S. W., Shields, G.A., 2019. Possible links between extreme oxygen perturbations and the Cambrian radiation of animals. Nature Geoscience 12, 468–473.

Hearing, T.W.W., Pohl, A., Williams, M., Donnadieu, Y., Harvey, T.H. P., Scotese, C.R., Sepulchre, P., Franc, A., Vandenbroucke, T.R.A., 2021. Quantitative comparison of geological data and model simulations constrains early Cambrian geography and climate. Nature Communications 12, 3868.

Hilton, R.G., West, A.J., 2020. Mountains, erosion and the carbon cycle. Nature Reviews Earth & Environment 1, 284–299.

Hindshaw, R.S., Tosca, R., Goût, T.L., Farnan, I., Tosca, N.J., Tipper, E. T., 2019. Experimental constraints on Li isotope fractionation during clay formation. Geochimica et Cosmochimica Acta 250, 219–237.

Huh, Y., Chan, L.H., Zhang, L., Edmond, J.M., 1998. Lithium and its isotopes in major world rivers: Implications for weathering and the oceanic budget. Geochimica et Cosmochimica Acta 62, 2039–2051.

Ihinger, P.D., Zink, S.I., 2000. Determination of relative growth rates of natural quartz crystals. Nature 404, 865–869.

Jiang, G.Q., Wang, X.Q., Shi, X.Y., Xiao, S.H., Zhang, S.H., Dong, J., 2012. The origin of decoupled carbonate and organic carbon isotope signatures in the early Cambrian (ca. 542–520 Ma) Yangtze platform. Earth and Planetary Science Letters 317, 96–110.

Kalderon-Asael, B., Katchinoff, J.A.R., Planavsky, N.J., Hood, A.V., Dellinger, M., Bellefroid, E.J., Jones, D.S., Hofmann, A., Ossa, F.O., Macdonald, F.A., Wang, C.J., Isson, T.T., Murphy, J.G., Higgins, J. A., West, A.J., Wallace, M.W., Asael, D., Pogge von Strandmann, P. A., 2021. A lithium-isotope perspective on the evolution of carbon and silicon cycles. Nature 595, 394–398.

Kolodny, Y., Chaussidon, M., 2005. Geochemistry of a chert breccia. Geochimica et Cosmochimica Acta 69, 427–439.

Kouchinsky, A., Bengtson, S., Runnegar, B., Skovsted, C., Steiner, M., Vendrasco, M., 2012. Chronology of early Cambrian biomineralization. Geological Magazine 149, 221–251.

Kump, L.R., Arthur, M.A., 1999. Interpreting carbon-isotope excursions: carbonates and organic matter. Chemical Geology 161, 181–198.

Kump, L.R., Brantley, S.L., Arthur, M.A., 2000. Chemical, weathering, atmospheric CO_2, and climate. Annual Review of Earth and Planetary Sciences 28, 611–667.

Li, C., Shi, W., Cheng, M., Jin, C.S., Algeo, T.J., 2020. The redox structure of Ediacaran and early Cambrian oceans and its controls. Science Bulletin 65, 2141–2149.

Li, G.J., Elderfield, H., 2013. Evolution of carbon cycle over the past 100 million years. Geochimica et Cosmochimica Acta 103, 11–25.

Li, G.J., West, A.J., 2014. Evolution of Cenozoic seawater lithium isotopes: Coupling of global denudation regime and shifting seawater sinks. Earth and Planetary Science Letters 401, 284–293.

Li, Z.H., Zhang, M., Chen, Z.Q., Algeo, T.J., Zhao, L.S., Zhang, F.F., 2021. Early Cambrian oceanic oxygenation and evolution of early animals: A critical review from the South China Craton. Global and Planetary Change 204, 103561.

Linnemann, U., Ovtcharova, M., Schaltegger, U., Gärtner, A., Hautmann, M., Geyer, G., Vickers-Rich, P., Rich, T., Plessen, B., Hofmann, M., Zieger, J., Krause, R., Kriesfeld, L., Smith, J., 2019. New high-resolution age data from the Ediacaran–Cambrian boundary indicate rapid, ecologically driven onset of the Cambrian explosion. Terra Nova 31, 49–58.

Liu, Z.R.R., Zhou, M.F., Wang, W., 2021. Mercury anomalies across the Ediacaran–Cambrian boundary: Evidence for a causal link between continental erosion and biological evolution. Geochimica et Cosmochimica Acta 304, 327–346.

Mackensen, A., Schmiedl, G., 2019. Stable carbon isotopes in paleoceanography: atmosphere, oceans, and sediments. Earth-Science Reviews 197, 102893.

Maloof, A.C., Ramezani, J., Bowring, S.A., Fike, D.A., Porter, S.M., Mazouad, M., 2010a. Constraints on early Cambrian carbon cycling from the duration of the Nemakit-Daldynian-Tommotian boundary $\delta^{13}C$ shift, Morocco. Geology 38, 623–626.

Maloof, A.C., Porter, S.M., Moore, J.L., Dudas, F.O., Bowring, S.A., Higgins, J.A., Fike, D.A., Eddy, M.P., 2010b. The earliest Cambrian record of animals and ocean geochemical change. Geological Society of America Bulletin 122, 1731–1774.

Mason, E., Edmonds, M., Turchyn, A.V., 2017. Remobilization of crustal carbon may dominate volcanic arc emissions. Science 357, 290–294.

McLennan, S.M., Hemming, S., McDaniel, D.K., Hanson, G.N., 1993. Geochemical approaches to sedimentation, provenance, and tectonics. In: Johnson, M.J., Basu, A. (Eds.), Processes Controlling the Composition of Clastic Sediments. Geological Society of America, Boulder, Colorado, pp. 21–40.

Misra, S., Froelich, P.N., 2012. Lithium isotope history of Cenozoic seawater: changes in silicate weathering and reverse weathering. Science 335, 818–823.

Molnar, P., Anderson, R.S., Anderson, S.P., 2007. Tectonics, fracturing of rock, and erosion. Journal of Geophysical Research: Earth Surface 112, F03014.

Myrow, P.M., Hughes, N.C., Goodge, J.W., Fanning, C.M., Williams, I. S., Peng, S.C., Bhargava, O.N., Parcha, S.K., Pogue, K.R., 2010. Extraordinary transport and mixing of sediment across Himalayan central Gondwana during the Cambrian-Ordovician. Geological Society of America Bulletin 122, 1660–1670.

Nesbitt, H.W., Young, G.M., 1982. Early Proterozoic climates and plate motions inferred from major element chemistry of lutites. Nature 299, 715–717.

Panahi, A., Young, G.M., Rainbird, R.H., 2000. Behavior of major and trace elements (including REE) during Paleoproterozoic pedogenesis and diagenetic alteration of an Archean granite near Ville Marie, Quebec, Canada. Geochimica et Cosmochimica Acta 64, 2199–2220.

Parnell, J., Armstrong, J.G.T., 2023. Surface expression of Late Caledonian magmatic lithium concentration, in the Rhynie Chert, UK. Geochemistry: Exploration, Environment, Analysis 23, geochem2023028.

Paytan, A., McLaughlin, K., 2007. The oceanic phosphorus cycle. Chemical Reviews 107, 563–576.

Peters, S.E., Gaines, R.R., 2012. Formation of the 'Great Unconformity' as a trigger for the Cambrian explosion. Nature 484, 363–366.
Planavsky, N.J., Rouxel, O.J., Bekker, A., Lalonde, S.V., Konhauser, K. O., Reinhard, C.T., Lyons, T.W., 2010. The evolution of the marine phosphate reservoir. Nature 467, 1088–1090.
Pogge von Strandmann, P.A., Desrochers, A., Murphy, M.J., Finlay, A.J., Selby, D., Lenton, T.M., 2017. Global climate stabilisation by chemical weathering during the Hirnantian glaciation. Geophysical Research Letters 3, 230–236.
Pogge von Strandmann, P.A., Schmidt, D.N., Planaysky, N.J., Wei, G.Y., Jones, C.L.C., Baumann, K.H., 2019. Assessing bulk carbonates as archives for seawater Li isotope ratios. Chemical Geology 530, 119338.
Pogge von Strandmann, P.A., Kasemann, S.A., Wimpenny, J.B., 2020. Lithium and lithium isotopes in Earth's surface cycles. Elements 16, 253–258.
Pogge von Strandmann, P.A., Jones, M.T., West, A.J., Murphy, M.J., Stokke, E.W., Tarbuck, G., Wilson, D.J., Pearce, C.R., Schmidt, D. N., 2021. Lithium isotope evidence for enhanced weathering and erosion during the Paleocene-Eocene Thermal Maximum. Science Advances 7, eabh4224.
Pruss, S.B., Gill, B.C., 2024. Life on the edge: The Cambrian marine realm and oxygenation. Annual Review of Earth and Planetary Sciences 52, 109–132.
Qie, W.K., Zhang, J.P., Luo, G.M., Algeo, T.J., Chen, B., Xiang, L., Liang, K., Liu, X.Y., Pogge von Strandmann, P.A., Chen, J.T., Wang, X.D., 2023. Enhanced continental weathering as a trigger for the End-Devonian Hangenberg crisis. Geophysical Research Letters 50, e2022GL102640.
Rothman, D.H., Hayes, J.M., Summons, R.E., 2003. Dynamics of the Neoproterozoic carbon cycle. Proceedings of the National Academy of Sciences of the United States of America 100, 8124–8129.
Rudnick, R.L., Gao, S., 2014. Composition of the continental crust. In: Holland, H.D., Turekian, K.K. (Eds.), Treatise on Geochemistry, Second Edition. Elsevier, Oxford, pp. 1–51.
Rugenstein, J.K.C., Ibarra, D.E., von Blanckenburg, F., 2019. Neogene cooling driven by land surface reactivity rather than increased weathering fluxes. Nature 571, 99–103.
Sauzéat, L., Rudnick, R.L., Chauvel, C., Garçon, M., Tang, M., 2015. New perspectives on the Li isotopic composition of the upper continental crust and its weathering signature. Earth and Planetary Science Letters 428, 181–192.
Schmitt, R.D.S., Fragoso, R.D.A., Collins, A.S., 2018. Suturing Gondwana in the Cambrian: The orogenic events of the final amalgamation. In: Siegfried, S., Basei, M.A.S., Orilol, P.O.S. (Eds.), Geology of Southwest Gondwana. Springer International Publishing, Cham, pp. 411–432.
Shen, B., Dong, L., Xiao, S.H., Lang, X.G., Huang, K.J., Peng, Y.B., Zhou, C.M., Ke, S., Liu, P.J., 2016. Molar tooth carbonates and benthic methane fluxes in Proterozoic oceans. Nature Communications 7, 10317.
Shields, G.A., Mills, B.J.W., 2017. Tectonic controls on the long-term carbon isotope mass balance. Proceedings of the National Academy of Sciences of the United States of America 114, 4318–4323.
Shields-Zhou, G., Zhu, M.Y., 2013. Biogeochemical changes across the Ediacaran–Cambrian transition in South China. Precambrian Research 225, 1–6.
Shu, D.G., Isozaki, Y., Zhang, X.L., Han, J., Maruyama, S., 2014. Birth and early evolution of metazoans. Gondwana Research 25, 884–895.
Squire, R.J., Campbell, I.H., Allen, C.M., Wilson, C.J.L., 2006. Did the Transgondwanan Supermountain trigger the explosive radiation of animals on Earth? Earth and Planetary Science Letters 250, 116–133.
Steinhoefel, G., Brantley, S.L., Fantle, M.S., 2021. Lithium isotopic fractionation during weathering and erosion of shale. Geochimica et Cosmochimica Acta 295, 155–177.
Sun, H., Xiao, Y.L., Gao, Y.J., Zhang, G.J., Casey, J.F., Shen, Y.A., 2018. Rapid enhancement of chemical weathering recorded by extremely light seawater lithium isotopes at the Permian–Triassic boundary. Proceedings of the National Academy of Sciences of the United States of America 115, 3782–3787.
Tessier, A., Campbell, P.G.C., Bisson, M., 1979. Sequential extraction procedure for the speciation of particulate trace-metals. Analytical Chemistry 51, 844–851.
Walker, J.C.G., Hays, P.B., Kasting, J.F., 1981. A negative feedback mechanism for the long-term stabilization of Earth's surface-temperature. Journal of Geophysical Research: Oceans 86, 9776–9782.
Wang, D., Ling, H.F., Struck, U., Zhu, X.K., Zhu, M.Y., He, T.C., Yang, B., Gamper, A., Shields, G.A., 2018. Coupling of ocean redox and animal evolution during the Ediacaran–Cambrian transition. Nature Communications 9, 2575.
Wang, J.G., Chen, D.Z., Yan, D.T., Wei, H.Y., Xiang, L., 2012. Evolution from an anoxic to oxic deep ocean during the Ediacaran–Cambrian transition and implications for bioradiation. Chemical Geology 306, 129–138.
Wang, J.S., Jiang, G.Q., Xiao, S.H., Li, Q., Wei, Q., 2008. Carbon isotope evidence for widespread methane seeps in the ca. 635 Ma Doushantuo cap carbonate in south China. Geology 36, 347–350.
Wang, W., Cawood, P.A., Pandit, M.K., Zhao, J.H., Zheng, J.P., 2019. No collision between Eastern and Western Gondwana at their northern extent. Geology 47, 308–312.
Wang, W., Cawood, P.A., Pandit, M.K., Xia, X.P., Raveggi, M., Zhao, J. H., Zheng, J.P., Qi, L., 2021. Fragmentation of South China from greater India during the Rodinia-Gondwana transition. Geology 49, 228–232.
Wei, G.Y., Planavsky, N.J., Tarhan, L.G., He, T.C., Wang, D., Shields, G.A., Wei, W., Ling, H.F., 2020. Highly dynamic marine redox state through the Cambrian explosion highlighted by authigenic $\delta^{238}U$ records. Earth and Planetary Science Letters 544, 116361.
Wei, G.Y., Zhao, M.Y., Sperling, E.A., Gaines, R.R., Kalderon-Asael, B., Shen, J., Li, C., Zhang, F.F., Li, G.J., Zhou, C.M., Cai, C.F., Chen, D. Z., Xiao, K.Q., Jiang, L., Ling, H.F., Planavsky, N.J., Tarhan, L.G., 2024. Lithium isotopic constraints on the evolution of continental clay mineral factory and marine oxygenation in the earliest Paleozoic Era. Science Advances 10, eadk2152.
Wei, T.Y., Cai, C.F., Xiong, Y.J., Bowyer, F.T., Poulton, S.W., in press. A nutrient control on fluctuating oceanic redox conditions during the Early Cambrian radiation of animals. Geology, doi: 10.1130/B38562.1.
West, A.J., Galy, A., Bickle, M., 2005. Tectonic and climatic controls on silicate weathering. Earth and Planetary Science Letters 235, 211–228.
Wood, R., Erwin, D.H., 2018. Innovation not recovery: dynamic redox promotes metazoan radiations. Biological Reviews 93, 863–873.
Xiang, L., Schoepfer, S.D., Shen, S.Z., Cao, C.Q., Zhang, H., 2017. Evolution of oceanic molybdenum and uranium reservoir size around the Ediacaran–Cambrian transition: Evidence from western Zhejiang, South China. Earth and Planetary Science Letters 464, 84–94.
Xiang, L., Schoepfer, S.D., Zhang, H., Cao, C.Q., Shen, S.Z., 2018. Evolution of primary producers and productivity across the Ediacaran–Cambrian transition. Precambrian Research 313, 68–77.
Yang, C., Zhu, M.Y., Condon, D.J., Li, X.H., 2017. Geochronological constraints on stratigraphic correlation and oceanic oxygenation in Ediacaran–Cambrian transition in South China. Journal of Asian Earth Sciences 140, 75–81.
Yao, J.L., Zhao, G.C., Han, Y.G., Liu, Q., Yu, S., Williams, S., He, Y.H., Li, Y., 2021. Establishment of modern plate tectonic regime and modern Earth system in the late Neoproterozoic–early Cambrian. Journal of Northwest University 51, 1007–1018 (in Chinese, with English abstract).
Ye, Y., Frings, P.J., von Blanckenburg, F., Feng, Q.L., 2021. Silicon isotopes reveal a decline in oceanic dissolved silicon driven by biosilicification: A prerequisite for the Cambrian Explosion? Earth and Planetary Science Letters 566, 116959.
Zhai, L.N., Wu, C.D., Ye, Y.T., Zhang, S.C., Wang, Y.Z., 2018. Fluctuations in chemical weathering on the Yangtze Block during the Ediacaran–Cambrian transition: Implications for paleoclimatic conditions and the marine carbon cycle. Palaeogeography, Palaeoclimatology, Palaeoecology 490, 280–292.

Zhang, F.F., Xiao, S.H., Kendall, B., Romaniello, S.J., Cui, H., Meyer, M., Gilleaudeau, G.J., Kaufman, A.J., Anbar, A.D., 2018. Extensive marine anoxia during the terminal Ediacaran Period. Science Advances 4, eaan8983.

Zhang, G.J., Chen, D.Z., Huang, K.J., Liu, M., Huang, T.Y., Yeasmin, R., Fu, Y., 2021. Dramatic attenuation of continental weathering during the Ediacaran–Cambrian transition: Implications for the climatic-oceanic-biological co-evolution. Global and Planetary Change 203, 103518.

Zhang, T.G., Chu, X.L., Zhang, Q.R., Feng, L.J., Huo, W.G., 2004. The sulfur and carbon isotopic records in carbonates of the Dengying Formation in the Yangtze Platform, China. Acta Petrologica Sinica 20, 717–724 (in Chinese, with English abstract).

Zhao, G.C., Cawood, P.A., 2012. Precambrian geology of China. Precambrian Research 222, 13–54.

Zhao, G.C., Wang, Y.J., Huang, B.C., Dong, Y.P., Li, S.Z., Zhang, G.W., Yu, S., 2018. Geological reconstructions of the East Asian blocks: From the breakup of Rodinia to the assembly of Pangea. Earth-Science Reviews 186, 262–286.

Zhao, T.X., Xu, S., Hao, F., 2023. Differential adsorption of clay minerals: Implications for organic matter enrichment. Earth-Science Reviews 246, 104598.

Zhu, M.Y., Strauss, H., Shields, G.A., 2007. From snowball earth to the Cambrian bioradiation: Calibration of Ediacaran–Cambrian earth history in South China. Palaeogeography, Palaeoclimatology, Palaeoecology 254, 1–6.

Zhu, M.Y., Zhao, F.C., Yin, Z.J., Zeng, H., Li, G.X., 2019. The Cambrian explosion: Advances and perspectives from China. Science China Earth Sciences 49, 1455–1490 (in Chinese).